



Fragmented phosphorus-doped graphitic carbon nitride nanoflakes with broad sub-bandgap absorption for highly efficient visible-light photocatalytic hydrogen evolution



Hua-Bin Fang^a, Xiao-Hong Zhang^a, Jiaojiao Wu^a, Nan Li^a, Yan-Zhen Zheng^{b,*}, Xia Tao^{a,*}

^a State Key Laboratory of Organic-Inorganic Composites, Beijing University of Chemical Technology, Beijing 100029, China

^b Research Center of the Ministry of Education for High Gravity Engineering & Technology, Beijing University of Chemical Technology, Beijing 100029, China

ARTICLE INFO

Keywords:

$\text{g-C}_3\text{N}_4$
Phosphorus doping
Fragmented nanoflakes
Sub-bandgap
Visible-light-driven H_2 evolution

ABSTRACT

Graphitic carbon nitride ($\text{g-C}_3\text{N}_4$) has shown great promise in photocatalytic solar-energy conversion. However, photocatalytic activity of pristine $\text{g-C}_3\text{N}_4$ still remains restricted owing to its low surface area, insufficient visible-light harvesting, and ready charge recombination. Here, fragmented P-doped $\text{g-C}_3\text{N}_4$ nanoflakes (PCNNFs), which are prepared by a facile two-step processing combining P-doping via using phytic acid biomass as P source and urea as $\text{g-C}_3\text{N}_4$ precursor and nanostructure tailoring via a smart post-treatment, are reported. Particularly, PCNNFs exhibit narrowed sub-bandgap from valence band to the midgap states, extending light absorption up to 800 nm. The resultant PCNNFs sample shows a surface area of $223.2 \text{ m}^2 \text{ g}^{-1}$, a highest value of P-doped $\text{g-C}_3\text{N}_4$ reported. The fragmented nanoflakes structure renders PCNNFs much shortened charge-to-surface migration distance in both vertical-plane and in-plane direction. Such PCNNFs are demonstrated to be highly efficient in charge transfer and separation. Attributed to the synergistic effect of P-doping and fragmented nanoflakes structure, PCNNFs exhibit a remarkable visible-light ($> 420 \text{ nm}$) photocatalytic H_2 production rate of $15921 \mu\text{mol h}^{-1} \text{ g}^{-1}$ and quantum efficiencies of 6.74% at 420 nm and 0.24% at 600 nm. Moreover, even under long wavelength light ($> 470 \text{ nm}$), PCNNFs still exhibit high H_2 production rate of $9546 \mu\text{mol h}^{-1} \text{ g}^{-1}$, over 62 times the rate of pure $\text{g-C}_3\text{N}_4$.

1. Introduction

In the search for robust and visible light active photocatalysts, a new class of polymeric semiconductor, graphitic carbon nitride ($\text{g-C}_3\text{N}_4$), has elicited ripples of excitement in the research communities due to its facile synthesis, appealing electronic band structure, high physico-chemical stability, and “earth-abundant” nature [1–6]. However, the pristine $\text{g-C}_3\text{N}_4$, which is prepared by directly thermal polymerization of common nitrogen-rich precursors, still suffers from unsatisfactory photocatalytic activity owing to its low surface area, restricted visible-light harvesting capacity, and ready recombination of charge carriers [7–9]. To date, various modification approaches, such as doping with heteroatoms [10–13], nanostructure design by hard-templating [14,15], exfoliation to two-dimensional nanosheets [16,17], supramolecular assembling [7,18,19], dye sensitization [20,21] and construction of $\text{g-C}_3\text{N}_4$ based heterojunctions [2,22–25], are adopted to enhance photocatalytic performance.

Doping as a process of introducing additional non-metal (e.g. B, S, F, P and I) or metal (e.g., Fe, Zn, K and Cu) atoms into $\text{g-C}_3\text{N}_4$ framework

to distinctly tune the optical and electronic properties of $\text{g-C}_3\text{N}_4$ is a predominant way to modulate bandgap structure and extend light absorption [2,10–13,26–32]. Generally, doping can extend the light absorption of $\text{g-C}_3\text{N}_4$ by reducing the optical bandgap i.e. the threshold for photons to be absorbed [33,34]. Most of the dopants for $\text{g-C}_3\text{N}_4$ only can reduce the bandgap by no more than 0.2 eV, corresponding to a minor increase in the onset for optical absorption of $\sim 45 \text{ nm}$ [2,33]. For instance, N-doping of $\text{g-C}_3\text{N}_4$ results in a decrease of the bandgap of less than 0.1 eV corresponding to broadening of optical absorption of $\sim 12 \text{ nm}$ [35]. F-doping of $\text{g-C}_3\text{N}_4$ results in bandgap decrease of 0.06 eV corresponding to broadening of optical absorption of $\sim 10 \text{ nm}$ [36]. A greater reduction in the bandgap was observed for P,O-co-doping, with a reduction of 0.17 eV corresponding to broadening of optical absorption of $\sim 38 \text{ nm}$ [37]. Apparently, the expanded light-harvesting capability derived from the bathochromic shift of the optical absorption band edge is rather limited [33]. Recently, there are a few reports mentioning light absorption expanding toward longer wavelength region via narrowing the sub-bandgap of $\text{g-C}_3\text{N}_4$ via P doping (i.e. from valence band (VB) to the midgap states located between

* Corresponding authors.

E-mail address: taoxia@mail.buct.edu.cn (X. Tao).

conduction band (CB) and VB) [10,38]. The narrowed sub-bandgap can absorb photons with energies smaller than the intrinsic bandgap of P-doped g-C₃N₄, thus resulting in long absorption tail (i.e. sub-bandgap absorption) [10,39]. Unlike the conventional bandgap narrowing, sub-bandgap narrowing has shown to be effective in expanding visible light absorption to much long wavelength. For instance, Qiao et al. [10] developed porous P-doped g-C₃N₄ nanosheets with sub-bandgap absorption by thermal poly-condensation of 2-aminoethylphosphonic acid and melamine mixture, exhibiting the extended light-responsive region up to 557 nm. It is worth noting that the formation, intensity or broadening of the sub-bandgap absorption of P-doped g-C₃N₄ photocatalysts are largely dependent on the synthetic conditions (such as P source, g-C₃N₄ precursor or preparation processing). Herein, we imagine if there is any possibility of achieving high-performance P-doped g-C₃N₄ photocatalyst with stronger and broader sub-bandgap absorption by seeking for more suitable P source and g-C₃N₄ precursor, and feasible treatment method.

In another aspect, textural engineering of g-C₃N₄ also has been developed to improve photocatalytic activities of g-C₃N₄ photocatalysts [14]. Various kinds of nanostructured g-C₃N₄ have already emerged, including porous g-C₃N₄ [40], g-C₃N₄ nanosheets [5] and g-C₃N₄ nanorods [41]. Converting bulk g-C₃N₄ into nanosheets has been proved to be an efficient strategy to obtain larger surface area, which may provide more exposed interfacial contact for the reactants and improve photocatalytic activity [5,16,42–45]. However, an intrinsic drawback of g-C₃N₄, i.e. the fast charge recombination, still is not well addressed, because converting bulk g-C₃N₄ into nanosheets only shortens the charge-to-surface migration distance in the vertical-plane direction but in the in-plane direction the charge-to-surface migration distance is still long. To shorten the charge-to-surface migration distance in the in-plane direction, g-C₃N₄ nanosheets need to be tailored into smaller-sized nanoflakes with rich in-plane edges. To this end, it is desirable to develop new post-treatment strategy to both exfoliating bulk g-C₃N₄ into nanosheets and tailoring the g-C₃N₄ nanosheets into smaller-sized nanoflakes with rich in-plane edges. Moreover, apart from the drawback of fast charge recombination, another drawback of g-C₃N₄ nanosheets is the strong quantum confinement effect i.e. bandgap of g-C₃N₄ increases when exfoliating bulk g-C₃N₄ into thin nanosheets, which restrains the visible light absorption [5,15]. Herein, to solve the problems above mentioned, we imagine constructing a fragmented P-doped g-C₃N₄ nanoflakes with ultrathin thickness, small plane size, and broad and strong sub-bandgap absorption. This is a strategy which can kill three birds with one stone, i.e. simultaneously achieving 1) much enlarged surface area; 2) shortened charge-to-surface migration distance in both vertical-plane and in-plane direction; 3) greatly enhanced visible light absorption by virtue of the broad and strong sub-bandgap absorption which overcomes the drawback brought by quantum confinement effect.

In this study, we develop a fragmented P-doped g-C₃N₄ nanoflakes (denoted as PCNNFs), which are prepared by a facile two-step processing combining P-doping via using phytic acid biomass as P source and urea as g-C₃N₄ precursor and nanostructure tailoring via a smart post-treatment. Specifically, P-doped g-C₃N₄ (PCN) is first prepared by directly thermal-condensation of phytic acid and urea mixture, then a successive phaco-fragmentation, freeze drying and thermal post-treatment is carried out for purpose of tailoring as-prepared PCN nanosheets to smaller-sized PCNNFs. Particularly, we find that PCNNFs exhibit narrowed sub-bandgap from VB to the midgap states and consequently extends the light absorption region up to 800 nm. The PCNNFs exhibit high surface area of 223.2 m² g⁻¹, a highest value of P-doped g-C₃N₄ reported. The fragmented nanoflakes structure renders PCNNFs much shortened charge-to-surface migration distance in both vertical-plane and in-plane direction. Such PCNNFs structure is demonstrated to be highly efficient in charge transfer and separation. As a consequence, PCNNFs achieve a remarkable enhanced visible light ($\lambda > 420$ nm) photocatalytic H₂ production rate of 15921 μmol h⁻¹ g⁻¹, far higher

than that of pure g-C₃N₄ (CN, 468 μmol h⁻¹ g⁻¹). Further, PCNNFs also exhibit a high H₂ production rate of 9546 μmol h⁻¹ g⁻¹ under light illumination with long wavelengths i.e. $\lambda > 470$ nm, which is over 62 times higher than that of CN (152 μmol h⁻¹ g⁻¹).

2. Experimental section

2.1. Preparation of PCN and PCNNFs

PCN was prepared by directly thermal-condensation method using phytic acid as P source and urea as g-C₃N₄ precursor. Firstly, 20 g urea (Beijing Shiji, A.R. 99%) and 0.04 g phytic acid (P108521-100 g, Aladdin) were thoroughly mixed. Then the mixture was placed in a porcelain crucible with a cover and wrapped carefully using aluminum foil. The wrapped porcelain crucible was placed in a muffle furnace and directly heated to 600 °C with a ramping rate of 3 °C/min in air and maintained at this temperature for 2 h. PCN was obtained after cooling to room temperature naturally. PCNNFs were prepared by an additional successive multistep post-treatment of PCN. The as-obtained PCN was phaco-fragmented in water for 15 min by an ultrasonic cell crusher (SCIENTZ-II D), and then the obtained products were freeze drying thoroughly using LABCONCO FreeZone 12 plus. Further, the products were moved to a porcelain crucible with cover and heated to 600 °C with a ramping rate of 10 °C/min in air and maintained at this temperature for 2 h. After cooling to room temperature naturally, PCNNFs were obtained. CN was prepared by the same procedure of preparing PCN except that no phytic acid was added to the precursor. PCN-x samples (x = 0.05% ~ 0.4%, representing the mass rate of phytic acid/urea) were obtained by adding different amount of phytic acid in the preparation process.

2.2. Characterizations

Fourier transform infrared (FTIR) spectra were measured on a Bruker Vertex 70v spectrometer. SEM images were characterized on a JEOL JSM-6701F field emission scanning electron microscope. TEM images were characterized on a Hitachi 7700 microscope. AFM measurements were performed on a Bruker Multimode 8 with ScanAsyst scanning probe microscope using Bruker SNL-10 probes. AFM-based infrared vibrational s-SNOM images of PCNNFs were obtained using a commercial scattering scanning near-field optical microscope (s-SNOM), the Inspire with PeakForce IR (Bruker Nano Surfaces). In the AFM based instrument the tip is illuminated via a monochromatic, tunable, low-noise quantum cascade laser (Daylight Solutions, San Diego, CA, USA). The tip-scattered light is then analyzed in an asymmetric Michelson interferometer with a two-phase homodyne detection scheme to directly obtain the nanoscale infrared absorption with a tip-limited spatial resolution of 10–20 nm. Metal-coated AFM tips (Nanoworld ARROW-NCPT-20) were used in tapping-mode. Background-free imaging was achieved via signal demodulation at 2nd harmonics of the tapping frequency. The BET specific surface area was taken using a Quantachrome Quadasorb SI automated surface area & pore size analyzer. Powder XRD analysis was performed on an X-ray diffractometer (X'Pert PRO MPD, Panalytical) using Cu K α radiation. XPS measurements were performed on an ESCALAB 250 (ThermoFisher Scientific USA) XPS spectrometer equipped with an Monochromated Al K α 150W X-ray Source. Solid state ³¹P MAS NMR measurements were carried out on a Bruker Avance 300 spectrometer. The spectra were recorded at a MAS spinning speed of 12 kHz while composite pulse decoupling was applied during the acquisition with a relaxation delay of 45s. The optical properties were studied using the adsorption spectra recorded on an ultraviolet-visible (UV-vis) spectrophotometer (Lambda 950 UV-vis). Photoluminescence (PL) spectra and time-resolved fluorescence decay spectra were obtained on a Spectrofluorometer FS5 (EDINBURGH INSTRUMENTS) with an excitation wavelength of 340 nm. Photoelectrochemical measurements

were performed in a standard three-electrode quartz cell with a 0.5 M Na₂SO₄ electrolyte solution. A platinum electrode and a saturated calomel electrode (SCE) were used as the counter electrode and the reference electrode, respectively. The EIS measurements were recorded at 0.01 V vs. SCE with ac amplitude of 5 mV and a frequency ranging from 0.1 Hz to 10 kHz. Photocurrent was measured at a 0 V bias. The photoelectrodes were prepared according to previously reported method using fluoride-tin oxide (FTO) as substrate [8]. Specifically, the FTO substrates were cleaned by ultrasonication in deionized water and absolute ethanol for 15 min, respectively, and then dried in an oven. 5 mg of photocatalyst and 10 µL of Nafion solution (5 wt%) were dispersed in 400 µL water/isopropanol mixed solvent (3:1 v/v) by 60 min sonication to prepare a homogeneous colloid. Then, the resultant catalyst colloid was deposited on the FTO conductive glass with area of ~1 cm² and then dried in air to form the photoelectrodes.

2.3. Photocatalytic activity measurements

Photocatalytic H₂ production experiments were performed using a top-irradiation vessel (Beijing China Education Au-Light Technology Co., Ltd, CEL-APR100). 10 mg of photocatalyst powder was dispersed in 100 mL aqueous solution containing 10 vol.% TEOA (T108154–500 mL, Aladdin) scavenger. 3 wt% Pt as the cocatalyst was in situ photo-deposited on the surface of photocatalysts using H₂PtCl₆ as a precursor. Before irradiation, the suspension was thoroughly degassed to remove air by bubbling N₂ for 30 min. The photocatalytic H₂ production was evaluated using a 300 W Xe lamp (Beijing China Education Au-Light Technology Co., Ltd, CEL-HXF300) equipped with needed cutoff filter. The evolved H₂ was analyzed by a gas chromatography (7890 B GC System, Agilent Technologies) with high-purity nitrogen carrier gas. The long-time photocatalytic H₂ production measurements were tested as follows. PCNNFs was used to catalyze the photocatalytic H₂ production for 50 h under a visible light irradiation ($\lambda > 420$ nm) using the method described above. The system was refreshed every 5 h by addition of 2 mL TEOA sacrificial agent and then bubbling N₂ for 30 min. The quantum efficiency (QE) of photocatalyst was measured using appropriate band pass filters (420 and 600 nm, respectively) to perform the H₂ production experiments under the designated monochromatic light. For the QE at 420 nm, the average intensity of irradiation was determined to be 80 mW/cm² and the irradiation area was 7.5 cm². For the QE at 600 nm, the average intensity of irradiation was measured to be 90 mW/cm² and the irradiation area was 7.5 cm². The QE values were calculated using the following equation:

$$\text{QE}(\%) = \frac{2 \times \text{number of evolved H}_2 \text{ molecules}}{\text{number of incident photons}} \times 100\%$$

2.4. Computational methods

The total energy calculations were performed using the projector augmented wave (PAW) pseudopotentials with the exchange and correlation in the Perdew-Burke-Ernzerhof (PBE) formalism of DFT as implemented in the Vienna ab initio simulation package (VASP). The unit cell is shown in Fig. S4; a cut-off energy of 400 eV and a Monkhorst-Pack k-mesh of 2 × 2 × 1 were used.

3. Results and discussion

PCNNFs were synthesized by a two-step process combining P-doping and further nanostructure tailoring as schematically illustrated in Fig. 1. Firstly, urea as g-C₃N₄ precursor and phytic acid as P source were thoroughly mixed and coupled by acid-base interaction and van der Waals' force [46]. The mixture was directly subjected to thermal-condensation under 600 °C, thus yielding PCN. Secondly, the as-prepared PCN was successively phaco-fragmented in water, dried by vacuum freeze drying, and then subjected to a further thermal treatment

under 600 °C to obtain PCNNFs. Fourier transform infrared (FTIR) spectra of PCN and PCNNFs (Fig. S1) show all the feature-distinctive stretch modes of aromatic C–N heterocycles between 1200–1700 cm⁻¹ together with the breathing mode of the heptazine units at ~810 cm⁻¹ [47,48], which are in good agreement with those of CN. These imply that PCN and PCNNFs remain the basic g-C₃N₄ chemical structure.

The morphological features of as-prepared samples were thoroughly investigated via scanning electron microscope (SEM), transmission electron microscope (TEM), atomic force microscopy (AFM) and infrared scattering-type scanning near-field optical microscopy (s-SNOM). SEM and TEM images show that both CN and PCN are composed of stacked sheet-like architecture (Fig. 2a–b & d–e). Notably, the PCNNFs sample features interlaced fragmentized nanoflakes structure (Fig. 2c & f), demonstrating that the PCN sheets successfully be tailored to fragmentized nanoflakes via the successive post-treatment processing. The smaller-sized PCNNFs apparently possess much shortened charge-to-surface migration distance in the in-plane direction. AFM images further confirm the morphology features of the three samples, that is, large-size nanosheets for CN and PCN and smaller-sized fragmented nanoflakes for PCNNFs (Fig. 3a, c & e). The thickness of CN, PCN and PCNNFs is determined to be 4.5–5.0 nm (Fig. 3b), 5.0–5.5 nm (Fig. 3d) and 1.5–4.0 nm (Fig. 3f), respectively. The thickness of PCN is slightly thicker than CN most probably owing to i) the larger radius of the doped P atom (100 pm) than that of the replaced C atom (70 pm) [10], and ii) the increased interlayer distance of PCN in comparison with CN as evidenced by XRD data (details see below). Notably, the thickness of PCNNFs is thinner than that of PCN, probably attributed to the stripping effect of the post-treatment processing. The ultrathin thickness renders PCNNFs much shortened charge-to-surface migration distance in the vertical-plane direction. Thus, the PCNNFs structure are believed to be more beneficial to charge mobility in the photocatalytic process due to their shortened charge-to-surface migration distance in both vertical-plane and in-plane direction. Infrared s-SNOM is a technique that enables to simultaneously provide topography and chemical group information of samples [49–51]. Fig. 3g–h shows the infrared vibrational s-SNOM images of PCNNFs with photon energy on- and off-resonance with the N–H deformation vibration. Apparently, the resonance signal of PCNNFs in Fig. 3h is in conformity with the AFM topography in Fig. 3e, further revealing the fragmentized nanoflakes structure of PCNNFs. There are strong resonance signals located on the edges of PCNNFs, and this means a large number of –NH– or –NH₂ terminals distributing on the edge sites of PCNNFs architecture. More details on the chemical microenvironments of PCNNFs will be further discussed in the following sections.

N₂ sorption isotherms of CN, PCN, and PCNNFs were investigated to obtain Brunauer–Emmett–Teller (BET) surface areas (Fig. 4a). As observed from the inset table, CN has a surface area of 68.9 m² g⁻¹, a common value of urea derived g-C₃N₄ [48,52]. Comparing with CN, PCN shows a reduced surface area of 58.1 m² g⁻¹. This is due to the relative thicker thickness of PCN nanosheets. After further being treated by the successive post-treatment processing, the resultant PCNNFs with ultrathin fragmentized nanoflakes structure show a much enhanced surface area of 223.2 m² g⁻¹, which outdistances the best value of the ever reported P-doped g-C₃N₄ [10].

X-ray diffraction (XRD) measurements were conducted to investigate the crystal structure of samples. As displayed in Fig. 4b, PCN and PCNNFs feature similar XRD patterns with CN, indicating that the original crystal structure of g-C₃N₄ is largely retained in PCNNFs and PCN. Furthermore, all three samples exhibit two diffraction peaks of (100) and (002), mainly attributed to the in-plane trigonal nitrogen linkage of tri-s-triazine motifs and the periodic stacking of layers of conjugated aromatic systems, respectively [6,48]. Note that the shifts of the characteristic (100) and (002) peaks are observed (inset of Fig. 4b). Compared with CN, PCN and PCNNFs show obvious shift of (100) peak from 12.80° to 12.73° to 12.57°, corresponding to the increase in the distance of in-planar nitride pores from 6.96 Å to 6.99 Å to 7.09 Å. In

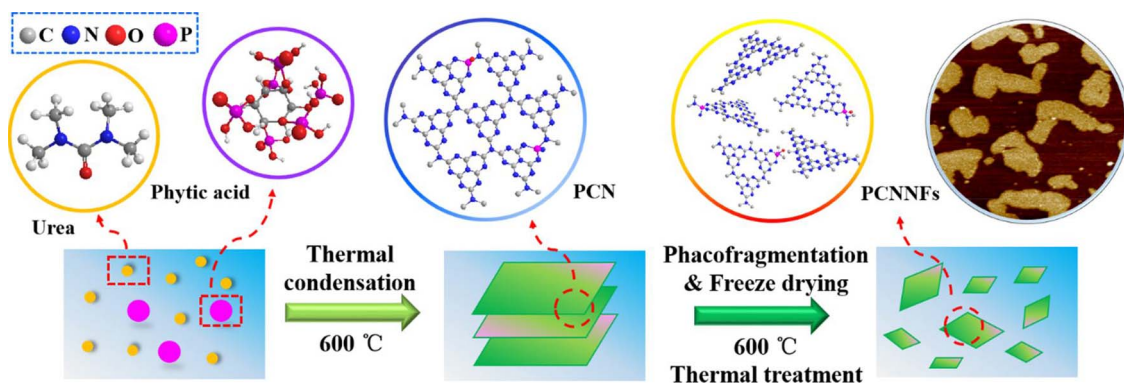


Fig. 1. Illustration of the preparation process of PCNNFs.

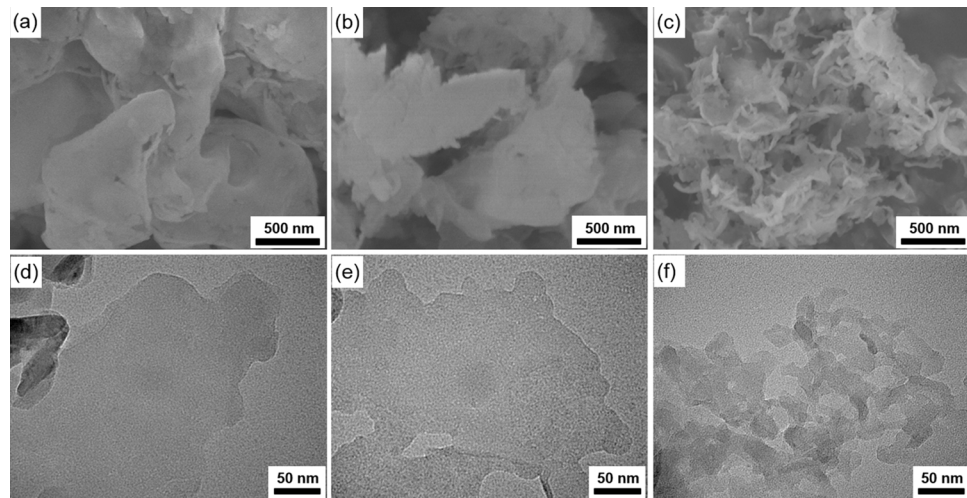
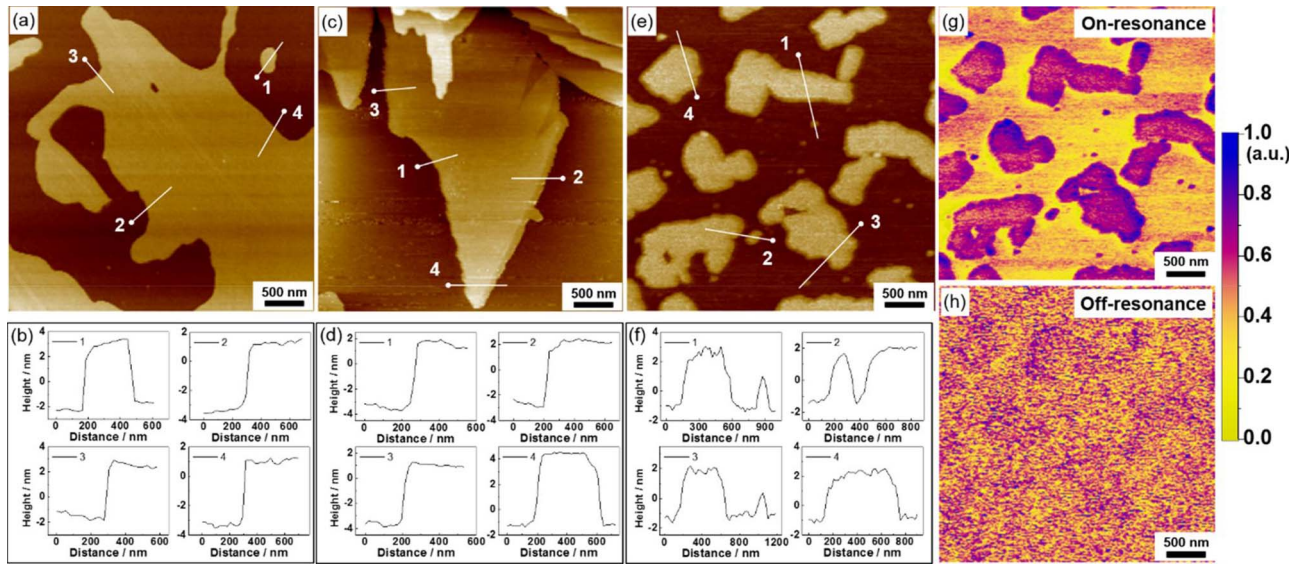


Fig. 2. SEM images of CN (a), PCN (b) and PCNNFs (c); TEM images of CN (d), PCN (e) and PCNNFs (f).

Fig. 3. AFM images and height profiles along the lines of CN (a, b), PCN (c, d) and PCNNFs (e, f). AFM-based infrared vibrational s-SNOM images of PCNNFs: on-resonance infrared near-field absorption at 1656 cm⁻¹ (g) and off-resonance absorption at 1750 cm⁻¹ (h).

comparison to CN, the (002) peak of PCN shifts negatively from 27.65° to 27.54°, and this suggests the increase of the interlayer distance from 3.22 Å to 3.24 Å after P doping. Such a negative shift and interlayer distance increase may be attributed to the larger radius of the doped P atom (100 pm) than that of the replaced C atom (70 pm) [10]. Further, the successive post-treatment of PCN leads to the shift of its (002) peak from 27.54° to 27.47° for PCNNFs, and this corresponds to the further

increase of the interlayer distance from 3.24 Å to 3.25 Å. This result is more likely to be due to looser packing of layers in PCNNFs via the successive post-treatment processing of PCN.

X-ray photoelectron spectroscopy (XPS) was used to investigate the specific surface composition and chemical bonding states of samples. The XPS survey spectra show the C1s peak at ~288 eV, N1s at ~399 eV, and O1s at ~532 eV for all samples and a weaker P2p peak at

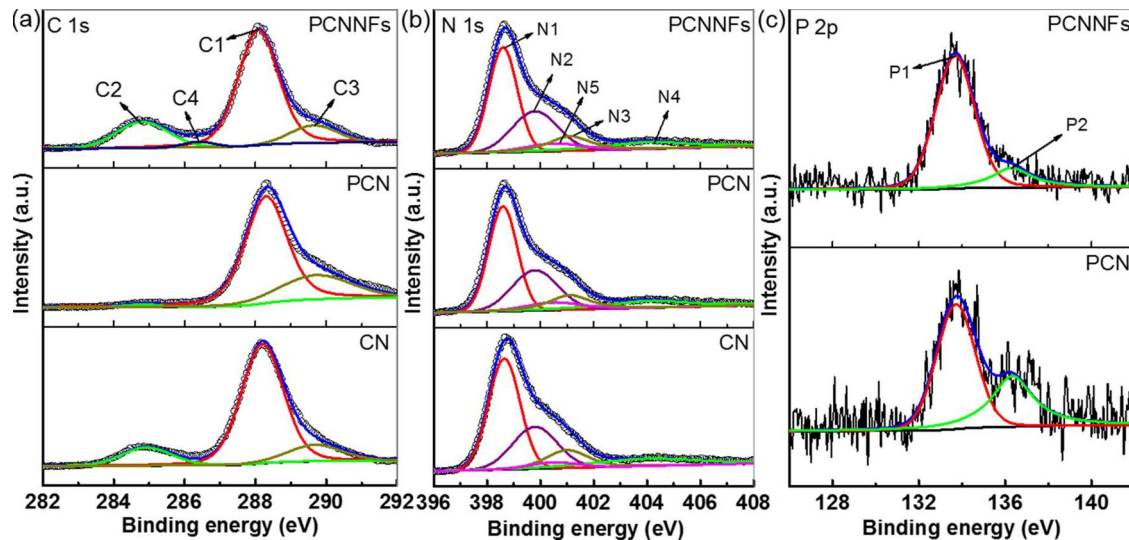
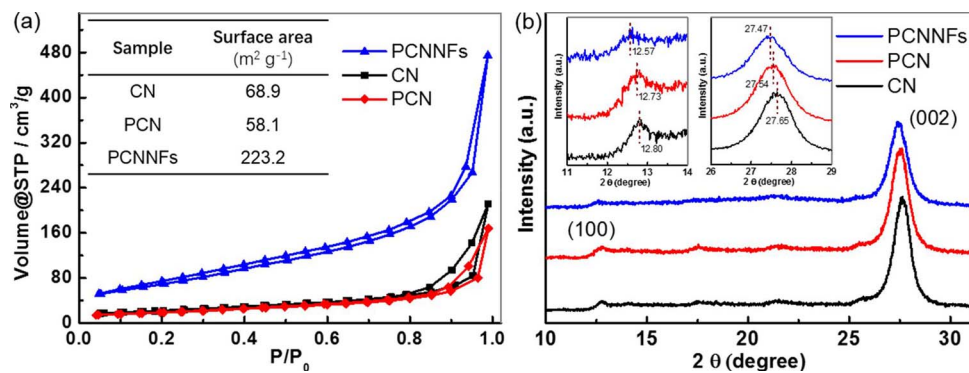


Fig. 5. High resolution C 1s (a), N 1s (b) and P 2p (c) XPS spectra of CN, PCN and PCNNFs.

~134 eV for PCN and PCNNFs (Fig. S2). The peak of O1s is mainly due to the oxygen originating from urea and/or air in the calcining process [48]. Fig. 5a–c shows high resolution XPS spectra of the C1s, N1s and P2p core levels. The C 1s spectra of all three samples (Fig. 5a) can be resolved into three peaks centered at 288.1 (C1), 284.8 (C2), and 289.6 (C3), which are attributed to $\text{N}=\text{C}(\text{N})_2$, graphitic C–C, and C–O, respectively [16,42,48]. Note that PCN has a lower area ratio of C2 than CN, mainly due to the introduction of phytic acid into the reaction system during the thermal polymerization process, while the C2 peak of PCNNFs i.e. graphitic C–C again becomes strong after the further thermal post-treatment (Table S1). Particularly, PCNNFs have a new peak at 286.4 eV (C4), which is ascribed to $\text{N}=\text{CH}-\text{N}$ terminals formed in the tailoring process from PCN to PCNNFs [8,53]. The N 1s spectra of the three samples (Fig. 5b) can be fitted to five discrete peaks, which are attributed to $\text{C}=\text{N}-\text{C}$ (N1, 398.6 eV), $\text{N}-(\text{C})_3$ (N2, 399.8 eV), $\text{C}-\text{NH}_2$ (N3, 401.1 eV), charging effects (N4, 404.0 eV) and $\text{C}-\text{NH}-\text{C}$ (N5, 400.5 eV) [48,54]. The P 2p signals of PCN and PCNNFs (Fig. 5c) can be separated into two peaks located at 133.7 eV (P1) and 136.3 eV (P2). Peak P1 is typical for P–N coordination [10,11,46,55–57]. Peak P2 can be correlated to P in high oxide states [57,58]. It is worth noting that no peak associated with P–C bonding (P–C coordination) would be ~1–2 eV lower than that of P–N bonding) in the XPS P 2p spectra of PCN and PCNNFs appears, implying that P most probably replaces C in the C–N framework of $\text{g-C}_3\text{N}_4$ to form P–N bonds [10,11,46,55,59]. There are two carbon sites, i.e. corner C and bay C in the tri-s-triazine unit of $\text{g-C}_3\text{N}_4$ (Fig. 6a). In this case, P atoms probably replace the corner C (P_{corner} configuration) or bay C (P_{bay} configuration) by P-doping. According to the calculation results reported by Yongfa Zhu's group [60], the corner C sites are more energy-favorable than the bay C

sites for P-doping in $\text{g-C}_3\text{N}_4$ network structure. To further verify the substitution sites of P atoms, we carried out the computations of the optimized pure $\text{g-C}_3\text{N}_4$, P_{bay} -doped $\text{g-C}_3\text{N}_4$ and P_{corner} -doped $\text{g-C}_3\text{N}_4$ configuration (Fig. S4). Our computational results show that in comparison with pure $\text{g-C}_3\text{N}_4$, the in-planar distance of nitride pores for the P_{bay} -doped $\text{g-C}_3\text{N}_4$ configuration is shortened to 7.18 Å from 7.25 Å, on the contrary, the in-planar distance of nitride pores for the P_{corner} -doped $\text{g-C}_3\text{N}_4$ configuration is elongated to 7.28 Å from 7.25 Å. This elongation in the P_{corner} -doped $\text{g-C}_3\text{N}_4$ configuration agrees well with the XRD results (i.e. enlarged nitride pore distances after P-doping) (Fig. 4b). The above data results and analysis provide more evidence for replacing corner C atoms by P atoms in the tri-s-triazine structure of PCN and PCNNFs.

^{31}P solid-state magic angle spinning nuclear magnetic resonance (MAS NMR) was conducted to explore the chemical environment of the P element doped in the tri-s-triazine network of PCN and PCNNFs. As shown in Fig. 6b, both the ^{31}P NMR spectra of PCN and PCNNFs exhibit two peaks at –0.8 and –12.4 ppm, which means at least two different chemical environment of P element existing in the tri-s-triazine network of PCN and PCNNFs. In addition, there are two new weak peaks at –28.1 and –41.3 ppm in the spectra of PCNNFs, which are most likely to be assigned to terminal P species formed in the process of tailoring PCN into PCNNFs.

The optical properties of samples were studied by UV-vis diffuse reflectance spectra (Fig. 6c), and the optical band gap energy (E_g) is acquired by the Kubelk–Munk method (Fig. 7) [39]. PCNNFs, PCN and CN show an equal E_g value of 3.03 eV, indicating that no intrinsic bandgap narrowing occurs in the processes of P-doping of $\text{g-C}_3\text{N}_4$ and the successive post-treatment of PCN. All the PCN-x samples with

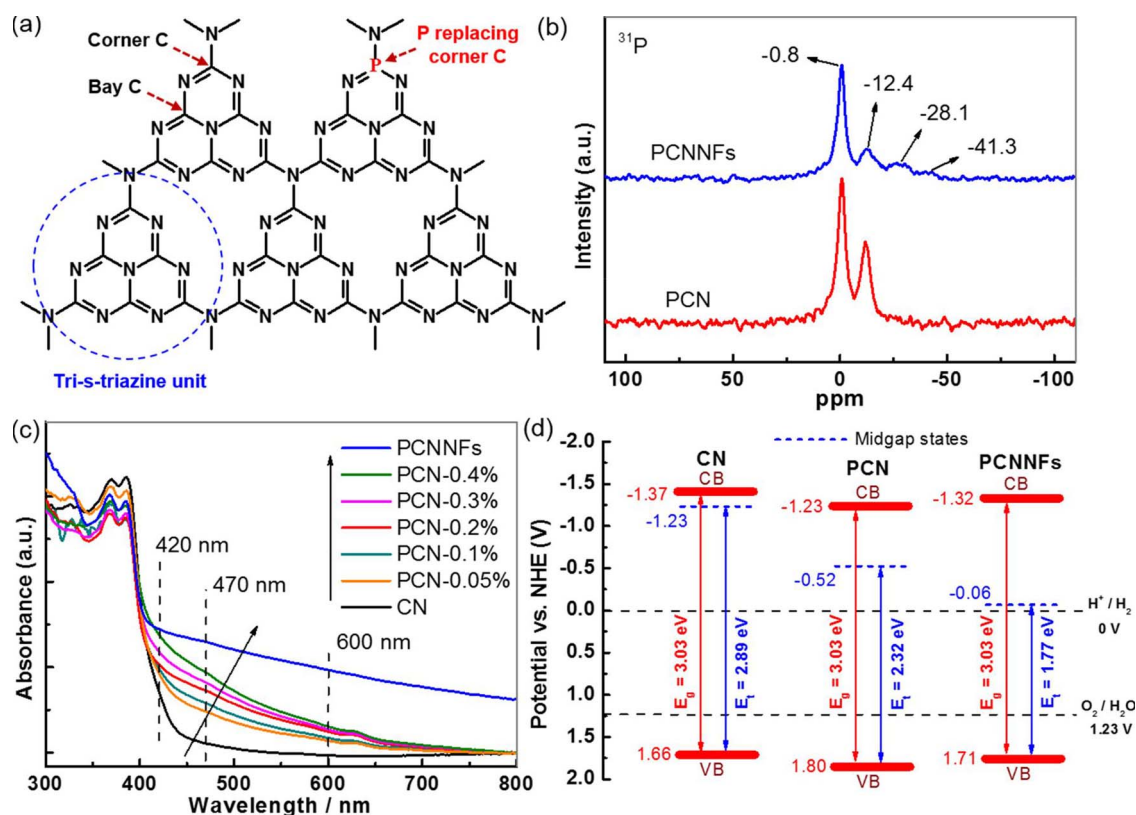


Fig. 6. (a) Diagram of g-C₃N₄ framework with P replacing corner C. (b) ³¹P MAS NMR spectra of PCN and PCNNFs. (c) UV-vis light absorption spectra of CN, PCN-x (x = 0.05–0.4%, representing the mass rate of phytic acid/urea, note that PCN-0.2% is also denoted as PCN elsewhere) and PCNNFs. (d) Electronic band structures of CN, PCN and PCNNFs.

different doping contents exhibit broad absorption tail (Urbach tail) extending the optical absorption region from 420 nm to 800 nm. Moreover, the absorbance of PCN samples increase with the increase of P contents. Interestingly, the Urbach tail of PCNNFs is further enhanced after tailoring PCN into PCNNFs by the post-treatment, which is attributed to the tailoring of polymeric network and texture of PCNNFs

and multiple inner reflections of the incident light within the fragmented nanoflakes architecture [15,47]. As reported, the Urbach tail is attributed to the electronic states located within the band gap, i.e. midgap states [10,39]. The strong and broad tail absorption can contribute significantly enhancement of the absorption of photons (known as sub-bandgap absorption) with energies lower than the intrinsic

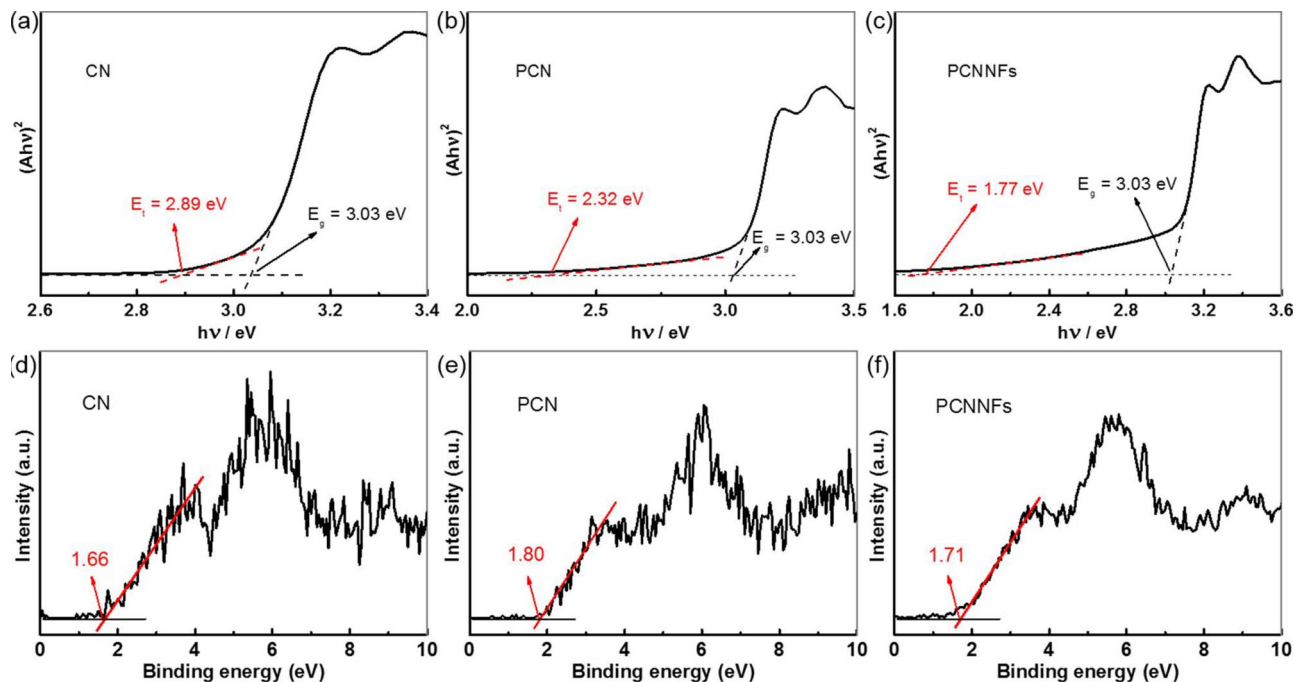


Fig. 7. The band gap energy (E_g) and transition energy (E_t) for CN (a), PCN (b) and PCNNFs (c). XPS valence band spectra of CN (d), PCN (e) and PCNNFs (f).

bandgap [39,61].

To reveal whether the sub-bandgap absorption of PCN and PCNNFs can promote photocatalytic H₂ evolution, it is essential to calculate the positions of midgap states in the bandgap. In this case, we firstly acquire the VB positions by XPS valence band spectra. As shown in Fig. 7, the VB positions of CN, PCN and PCNNFs are determined as 1.66, 1.80 and 1.71 V vs. NHE, respectively. Then the CB positions of samples are obtained according to the common equation [38]:

$$E_{CB} = E_{VB} - E_g$$

where the E_{CB} and E_{VB} represent the CB and VB positions, respectively. Thus, the CB positions of CN, PCN and PCNNFs are calculated as –1.37, –1.23 and –1.32 V vs. NHE, respectively. The transition energy (E_t) from VB to the midgap states are calculated to be 2.89 eV (CN), 2.32 eV (PCN) and 1.77 eV (PCNNFs) by the Kubelk-Munk method in Fig. 7 [10,39]. Finally, as shown in Fig. 6d, the position of midgap states for CN, PCN and PCNNFs are determined to be –1.23, –0.52 and –0.06 V vs. NHE. Each value is more negative than the H₂ evolving level ($2H^+ + 2e^- = H_2, E^0 = 0 \text{ V vs. NHE}$) [16], suggesting that the photo-generated electrons excited from VB to the midgap states are capable of reducing protons to evolve H₂ in thermodynamics.

Apart from light absorption, photo-excited electron-hole separation and charge transfer are also key factors for photocatalysis [14,62]. Photoluminescence (PL) emission spectrum is a powerful tool to characterize the radiative recombination process of photo-excited carriers in a photocatalyst [8,47]. As shown in Fig. 8a, in contrast to a strong fluorescence emission peak exhibited by CN, PCN-x and PCNNFs present much quenched PL signals, indicating more efficient separation of charge carries for PCN-x and PCNNFs. Specifically, when the P-doping contents increase from 0.05% to 0.2%, the PL signals of PCN-x gradually decrease corresponding to suppressed recombination of the photo-induced charge carriers [8]. Further increase the P-doping contents (maximum up to 0.4%) causes an increase of PL signals, suggesting

enhanced recombination of electron-hole pairs caused by the excess amounts of P dopants as the recombination centers [31]. Moreover, the PL signal of PCNNFs is obviously lower than that of PCN-x, suggesting the higher separation efficiency of PCNNFs owing to the structural benefits of PCNNFs i.e. much shortened charge-to-surface migration distance in both vertical-plane and in-plane direction. Notably, the emission peaks of PCN and PCNNFs display red shift, which is associated with the narrowed sub-bandgap of PCN and PCNNFs [17,63]. The fluorescence emission based on narrower sub-bandgap accordingly red-shift toward longer wavelength [54,63]. To further understand the photophysical behaviors of the photo-excited charge carriers, the time-resolved fluorescence decay spectra of CN, PCN and PCNNFs were recorded (Fig. S5). The fitting PL decay data and average life-time (τ_{avg}) of CN, PCN and PCNNFs are summarized and listed in Table S2. According to the calculated results, the τ_{avg} of charge carries decreases from 4.80 ns of CN to 3.09 ns of PCN to 2.55 ns of PCNNFs. The lowest τ_{avg} for PCNNFs further implies the efficient charge separation and transfer occurring in the fragmented nanoflakes structure of PCNNFs [64,65], which is consistent with the PL quenching results. The charge transfer, which is believed to be concerned with charge separation, is also evaluated by electrochemical impedance spectroscopy (EIS), and the results are shown in Fig. 8b. The radius of the arc in the EIS spectra reflects the interface layer resistance occurring at the electrode surface, and a smaller arc radius implies a lower charge transfer resistance [62,66–68]. The charge transfer resistance follows a trend in a sequence of PCNNFs < PCN < CN, suggesting charge transfer efficiency in the order of PCNNFs > PCN > CN. The charge separation and transfer efficiency are also reflected in the transient photocurrent measurements (Fig. 8c), where the photocurrent follows a trend in a sequence of PCNNFs > PCN > CN. The enhancement of photocurrent further demonstrates that the P doping and the fragmented nanoflakes structure can synergistically improve the charge separation and transfer efficiency of PCNNFs, in accordance with the results of PL and EIS analysis.

The photocatalytic activities for H₂ production of as-prepared

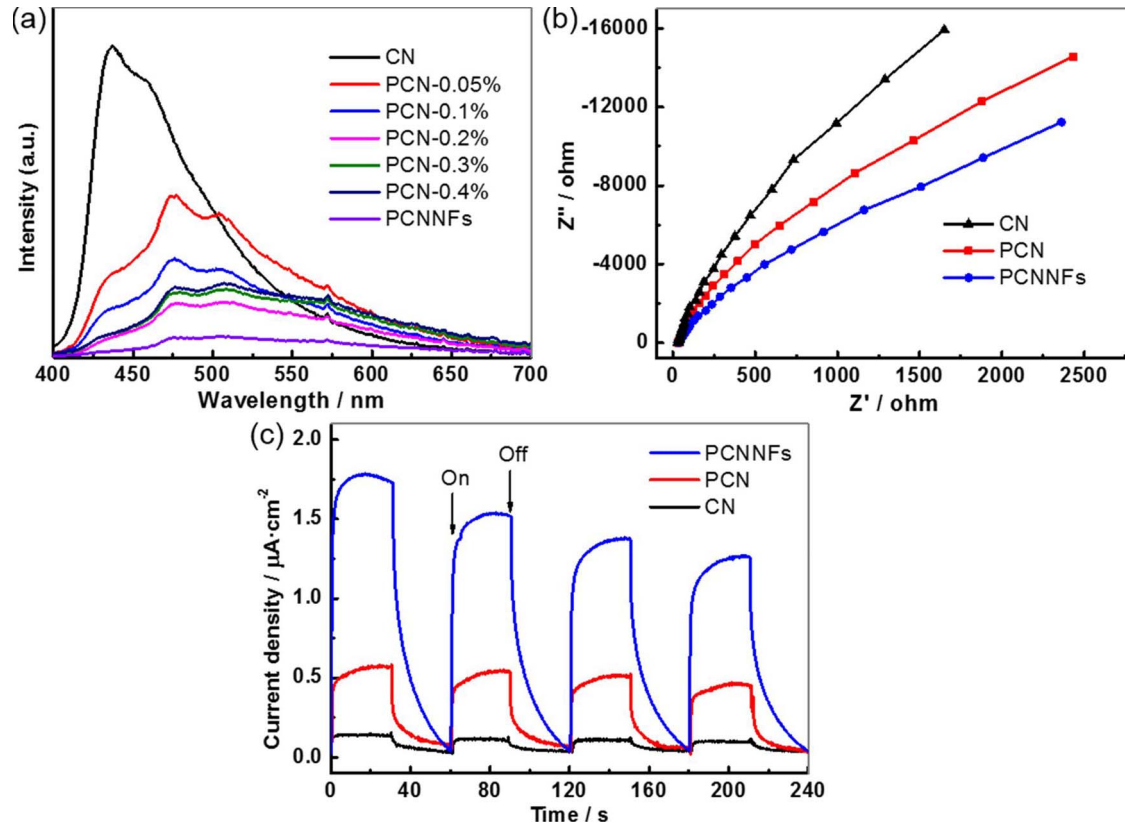


Fig. 8. (a) PL spectra of CN, PCN-x and PCNNFs. (b) EIS Nyquist plots, and (c) Visible light ($\lambda > 420 \text{ nm}$) induced transient photocurrent responses of CN, PCN and PCNNFs.

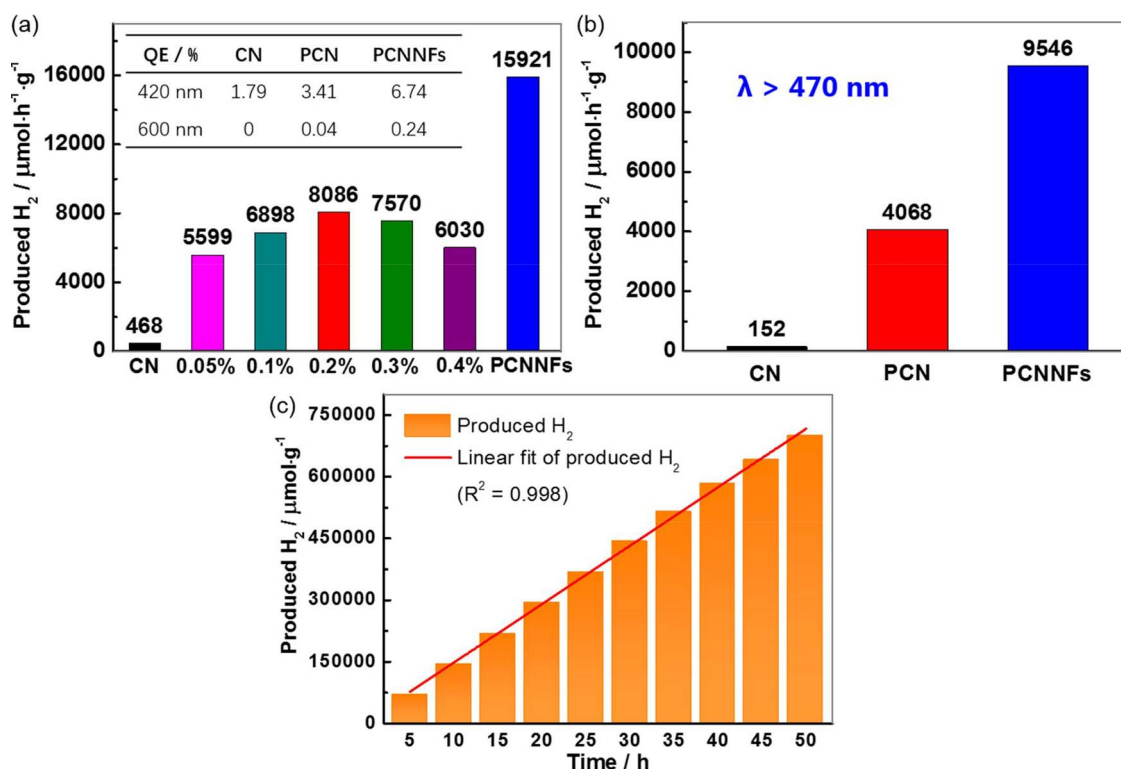


Fig. 9. (a) Photocatalytic H_2 evolution rates for CN, PCN-x and PCNNFs under visible light irradiation ($\lambda > 420 \text{ nm}$), and QE at $\lambda = 420 \text{ nm}$ and 600 nm of CN, PCN and PCNNFs (inset). (b) Photocatalytic H_2 production rates for CN, PCN and PCNNFs under long wavelength light irradiation ($\lambda > 470 \text{ nm}$). (c) Photocatalytic H_2 production catalyzed by PCNNFs under a prolonged visible light irradiation ($\lambda > 420 \text{ nm}$) of 50 h.

samples were evaluated using Pt as cocatalyst and triethanolamine (TEOA) as hole scavenger. Fig. 9a shows the comparison of photocatalytic H_2 production activities of CN, PCN-x and PCNNFs under visible light ($\lambda > 420 \text{ nm}$). The CN sample only exhibits a very low photocatalytic H_2 production rate of $468 \mu\text{mol}\cdot\text{h}^{-1}\cdot\text{g}^{-1}$, arising from its limited visible-light absorption, low surface area and poor charge separation and transfer capability. After introducing P with different contents into g-C₃N₄ i.e. PCN-x, the photocatalytic H_2 production activities of PCN-x increase markedly in comparison with CN. Specifically, when the P-doping contents increase from 0.05% to 0.2%, the H_2 production rates of PCN-x gradually increase, but further increase (maximum up to 0.4%) causes a decrease of H_2 production rate owing to that the excess amounts of dopants are considered as recombination centers to inhibit the separation of photo-induced electron-hole pairs [69]. Remarkably, PCNNFs show the highest photocatalytic H_2 production rate of $15921 \mu\text{mol}\cdot\text{h}^{-1}\cdot\text{g}^{-1}$, which is over 34 times higher than that of CN. The excellent photocatalytic performance of PCNNFs can also be reviewed through the quantum efficiency (QE) data (inset Fig. 9a). PCNNFs shows a high QE of 6.74% at 420 nm and a QE of 0.24% at 600 nm. In contrast, CN shows no QE at the wavelength of 600 nm because of no light absorption at such a wavelength. To better reveal the photocatalytic response at the long wavelength region of visible light, H_2 production experiments were carried out using a long-pass cutoff filter allowing $\lambda > 470 \text{ nm}$. As shown in Fig. 9b, the H_2 production rate of PCNNFs is $9546 \mu\text{mol}\cdot\text{h}^{-1}\cdot\text{g}^{-1}$, which is over 2 times higher than that of PCN ($4068 \mu\text{mol}\cdot\text{h}^{-1}\cdot\text{g}^{-1}$), and over 62 times higher than that of CN. These results clearly demonstrated that P doping and further post-treatment into fragmented nanoflakes can synergistically and very efficiently improve the performance of visible light photocatalytic H_2 production of PCNNFs by virtue of strong and broad sub-bandgap absorption, efficient charge separation and transfer, and enlarged surface area as demonstrated above.

Additionally, the stability of a photocatalyst is also very important from the point of view of its practical application. In order to check the

stability, we carried out photocatalytic H_2 production catalyzed by PCNNFs under a prolonged visible light irradiation ($\lambda > 420 \text{ nm}$) of 50 h (Fig. 9c). No obvious decay of photocatalytic H_2 production is observed, indicating the robustness of PCNNFs. To further confirm the photostability of PCNNFs, we compare the XRD patterns and TEM images of PCNNFs sample before and after the prolonged photocatalytic H_2 production experiment (Figs. S6 & S7). It is found that PCNNFs sample has no obvious changes in the crystalline structure and morphology after the prolonged photocatalytic H_2 production experiment, demonstrating the good stability of PCNNFs.

4. Conclusion

In conclusion, PCNNFs were successfully synthesized by a two-step process combining P doping via thermal-condensation of phytic acid and urea mixture and further nanostructure tailoring via a successive phacofragmentation, freeze drying and thermal post-treatment. Attributed to the synergistic effect of P-doping and fragmented nanoflakes structure, PCNNFs show strong sub-bandgap absorption in the whole visible region, much enlarged the surface area and improved charge separation and transfer efficiency. As a consequence, PCNNFs exhibit remarkable visible-light ($> 420 \text{ nm}$) photocatalytic H_2 production rate of $15921 \mu\text{mol}\cdot\text{h}^{-1}\cdot\text{g}^{-1}$ and quantum efficiencies of 6.74% at 420 nm and 0.24% at 600 nm. Even under long wavelength light ($> 470 \text{ nm}$), PCNNFs still exhibit high H_2 production rate of $9546 \mu\text{mol}\cdot\text{h}^{-1}\cdot\text{g}^{-1}$, over 62 times the rate of CN. Such a stable high-performance visible light photocatalyst representing one of the most highly active g-C₃N₄ based photocatalyst.

Acknowledgements

The work was supported by the National Natural Science Foundation of China (Nos. 21476019, 21377011, 21676017). The authors also thanked Meilan Huang and Jianming Yue for helping in the

theoretical calculation.

Appendix A. Supplementary data

Supplementary data associated with this article can be found, in the online version, at <https://doi.org/10.1016/j.apcatb.2017.11.080>.

References

- [1] X. Wang, K. Maeda, A. Thomas, K. Takanabe, G. Xin, J.M. Carlsson, K. Domen, M. Antonietti, *Nat. Mater.* 8 (2009) 76–80.
- [2] W.J. Ong, L.L. Tan, Y.H. Ng, S.T. Yong, S.P. Chai, *Chem. Rev.* 116 (2016) 7159–7329.
- [3] S. Cao, J. Low, J. Yu, M. Jaroniec, *Adv. Mater.* 27 (2015) 2150–2176.
- [4] J. Liu, H. Wang, M. Antonietti, *Chem. Soc. Rev.* 45 (2016) 2308–2326.
- [5] J. Zhang, Y. Chen, X. Wang, *Energy Environ. Sci.* 8 (2015) 3092–3108.
- [6] J. Liu, Y. Liu, N. Liu, Y. Han, X. Zhang, H. Huang, Y. Lifshitz, S.-T. Lee, J. Zhong, Z. Kang, *Science* 347 (2015) 970–974.
- [7] Y.-S. Jun, E.Z. Lee, X. Wang, W.H. Hong, G.D. Stucky, A. Thomas, *Adv. Funct. Mater.* 23 (2013) 3661–3667.
- [8] G. Liu, G. Zhao, W. Zhou, Y. Liu, H. Pang, H. Zhang, D. Hao, X. Meng, P. Li, T. Kako, J. Ye, *Adv. Funct. Mater.* 26 (2016) 6822–6829.
- [9] Y. Zheng, L. Lin, B. Wang, X. Wang, *Angew. Chem. Int. Ed.* 54 (2015) 12868–12884.
- [10] J. Ran, T.Y. Ma, G. Gao, X.-W. Du, S.Z. Qiao, *Energy Environ. Sci.* 8 (2015) 3708–3717.
- [11] S. Guo, Z. Deng, M. Li, B. Jiang, C. Tian, Q. Pan, H. Fu, *Angew. Chem. Int. Ed.* 55 (2016) 1830–1834.
- [12] G. Zhang, M. Zhang, X. Ye, X. Qiu, S. Lin, X. Wang, *Adv. Mater.* 26 (2014) 805–809.
- [13] K. Wang, Q. Li, B. Liu, B. Cheng, W. Ho, J. Yu, *Appl. Catal. B* 176 (2015) 44–52.
- [14] J. Zhang, M. Zhang, C. Yang, X. Wang, *Adv. Mater.* 26 (2014) 4121–4126.
- [15] J. Sun, J. Zhang, M. Zhang, M. Antonietti, X. Fu, X. Wang, *Nat. Commun.* 3 (2012) 1139.
- [16] Q. Han, B. Wang, J. Gao, Z. Cheng, Y. Zhao, Z. Zhang, L. Qu, *ACS Nano* 10 (2016) 2745–2751.
- [17] P. Niu, L. Zhang, G. Liu, H.-M. Cheng, *Adv. Funct. Mater.* 22 (2012) 4763–4770.
- [18] J. Xu, S. Cao, T. Brenner, X. Yang, J. Yu, M. Antonietti, M. Shalom, *Adv. Funct. Mater.* 25 (2015) 6265–6271.
- [19] M. Shalom, S. Inal, C. Fettkenhauer, D. Neher, M. Antonietti, *J. Am. Chem. Soc.* 135 (2013) 7118–7121.
- [20] Y. Wang, J. Hong, W. Zhang, R. Xu, *Catal. Sci. Technol.* 3 (2013) 1703–1711.
- [21] S. Min, G. Lu, *J. Phys. Chem. C* 116 (2012) 19644–19652.
- [22] D.J. Martin, P.J. Reardon, S.J. Moniz, J. Tang, *J. Am. Chem. Soc.* 136 (2014) 12568–12571.
- [23] R. Ye, H. Fang, Y.Z. Zheng, N. Li, Y. Wang, X. Tao, *ACS Appl. Mater. Interfaces* 8 (2016) 13879–13889.
- [24] W. Wang, J.C. Yu, D. Xia, P.K. Wong, Y. Li, *Environ. Sci. Technol.* 47 (2013) 8724–8732.
- [25] G. Dong, L. Yang, F. Wang, L. Zang, C. Wang, *ACS Catal.* 6 (2016) 6511–6519.
- [26] Y. Zhou, L. Zhang, J. Liu, X. Fan, B. Wang, M. Wang, W. Ren, J. Wang, M. Li, J. Shi, *J. Mater. Chem. A* 3 (2015) 3862–3867.
- [27] Y. Wang, H. Li, J. Yao, X. Wang, M. Antonietti, *Chem. Sci.* 2 (2011) 446–450.
- [28] Z. Lin, X. Wang, *Angew. Chem. Int. Ed.* 52 (2013) 1735–1738.
- [29] L.-F. Gao, T. Wen, J.-Y. Xu, X.-P. Zhai, M. Zhao, G.-W. Hu, P. Chen, Q. Wang, H.-L. Zhang, *ACS Appl. Mater. Interfaces* 8 (2015) 617–624.
- [30] Z. Li, C. Kong, G. Lu, *J. Phys. Chem. C* 120 (2015) 56–63.
- [31] Y. Guo, T. Chen, Q. Liu, Z. Zhang, X. Fang, *J. Phys. Chem. C* 120 (2016) 25328–25337.
- [32] M. Zhang, X. Bai, D. Liu, J. Wang, Y. Zhu, *Appl. Catal. B* 164 (2015) 77–81.
- [33] S.A. Shevlin, Z.X. Guo, *Chem. Mater.* 28 (2016) 7250–7256.
- [34] Q. Guo, Y. Zhang, J. Qiu, G. Dong, *J. Mater. Chem. C* 4 (2016) 6839–6847.
- [35] J. Fang, H. Fan, M. Li, C. Long, *J. Mater. Chem. A* 3 (2015) 13819–13826.
- [36] Y. Wang, Y. Di, M. Antonietti, H. Li, X. Chen, X. Wang, *Chem. Mater.* 22 (2010) 5119–5121.
- [37] J. Li, B. Shen, Z. Hong, B. Lin, B. Gao, Y. Chen, *Chem. Commun.* 48 (2012) 12017.
- [38] Y. Deng, L. Tang, G. Zeng, Z. Zhu, M. Yan, Y. Zhou, J. Wang, Y. Liu, J. Wang, *Appl. Catal. B* 203 (2017) 343–354.
- [39] H. Yaghoubi, Z. Li, Y. Chen, H.T. Ngo, V.R. Bheethanabotla, B. Joseph, S. Ma, R. Schlaf, A. Takshi, *ACS Catal.* 5 (2015) 327–335.
- [40] H.-B. Fang, Y. Luo, Y.-Z. Zheng, W. Ma, X. Tao, *Ind. Eng. Chem. Res.* 55 (2016) 4506–4514.
- [41] X. Bai, L. Wang, R. Zong, Y. Zhu, *J. Phys. Chem. C* 117 (2013) 9952–9961.
- [42] Q. Han, B. Wang, Y. Zhao, C. Hu, L. Qu, *Angew. Chem. Int. Ed.* 54 (2015) 11433–11437.
- [43] Y. Li, R. Jin, Y. Xing, J. Li, S. Song, X. Liu, M. Li, R. Jin, *Adv. Energy Mater.* 6 (2016) 1601273.
- [44] M.J. Lima, A.M.T. Silva, C.G. Silva, J.L. Faria, *J. Catal.* 353 (2017) 44–53.
- [45] J. Xu, Z. Wang, Y. Zhu, *ACS Appl. Mater. Interfaces* 9 (2017) 27727–27735.
- [46] T.Y. Ma, J. Ran, S. Dai, M. Jaroniec, S.Z. Qiao, *Angew. Chem. Int. Ed.* 54 (2015) 4646–4650.
- [47] Q. Liang, Z. Li, Z.-H. Huang, F. Kang, Q.-H. Yang, *Adv. Funct. Mater.* 25 (2015) 6885–6892.
- [48] D.J. Martin, K. Qiu, S.A. Shevlin, A.D. Handoko, X. Chen, Z. Guo, J. Tang, *Angew. Chem. Int. Ed.* 53 (2014) 9240–9245.
- [49] K.M. Carneiro, H. Zhai, L. Zhu, J.A. Horst, M. Sitlin, M. Nguyen, M. Wagner, C. Simpliciano, M. Milder, C.L. Chen, P. Ashby, J. Bonde, W. Li, S. Habelitz, *Sci. Rep.* 6 (2016) 23105.
- [50] B. Pollard, E.A. Muller, K. Hinrichs, M.B. Raschke, *Nat. Commun.* 5 (2014) 3587.
- [51] A. Dazzi, C.B. Prater, Q. Hu, D.B. Chase, J.F. Rabolt, C. Marcott, *Appl. Spectrosc.* 66 (2012) 1365–1384.
- [52] Y. Zhang, J. Liu, G. Wu, W. Chen, *Nanoscale* 4 (2012) 5300–5303.
- [53] P. Niu, L.C. Yin, Y.Q. Yang, G. Liu, H.M. Cheng, *Adv. Mater.* 26 (2014) 8046–8052.
- [54] Q. Han, B. Wang, J. Gao, L. Qu, *Angew. Chem. Int. Ed.* 55 (2016) 10849–10853.
- [55] Y. Zhang, M. Antonietti, *J. Am. Chem. Soc.* 5 (2010) 1307–1311.
- [56] D.-H. Lan, H.-T. Wang, L. Chen, C.-T. Au, S.-F. Yin, *Carbon* 100 (2016) 81–89.
- [57] L.S. Dako, D.R. Baer, D.M. Friedrich, J. Vac. Sci. Technol. A 7 (1989) 1634–1638.
- [58] J.P. Paraknowitsch, Y. Zhang, B. Wienert, A. Thomas, *Chem. Commun.* 49 (2013) 1208–1210.
- [59] Y.P. Zhu, T.Z. Ren, Z.Y. Yuan, *ACS Appl. Mater. Interfaces* 7 (2015) 16850–16856.
- [60] X. Ma, Y. Lv, J. Xu, Y. Liu, R. Zhang, Y. Zhu, *J. Phys. Chem. C* 116 (2012) 23485–23493.
- [61] P. Nagpal, V.I. Klimov, *Nat. Commun.* 2 (2011) 486.
- [62] H.-B. Fang, N. Li, Z. Xue, Y. Zhang, Y.-Z. Zheng, X. Tao, *Electrochim. Commun.* 72 (2016) 118–121.
- [63] J. Zhang, G. Zhang, X. Chen, S. Lin, L. Mohlmann, G. Dolega, G. Lipner, M. Antonietti, S. Blechert, X. Wang, *Angew. Chem. Int. Ed. Engl.* 51 (2012) 3183–3187.
- [64] C. Li, Y. Du, D. Wang, S. Yin, W. Tu, Z. Chen, M. Kraft, G. Chen, R. Xu, *Adv. Funct. Mater.* 27 (2017) 1604328.
- [65] P. Qiu, C. Xu, H. Chen, F. Jiang, X. Wang, R. Lu, X. Zhang, *Appl. Catal. B* 206 (2017) 319–327.
- [66] X.-H. Lu, Y.-Z. Zheng, S.-Q. Bi, Y. Wang, X. Tao, L. Dai, J.-F. Chen, *Adv. Energy Mater.* 4 (2014) 1301802.
- [67] Y. Wang, Y.Z. Zheng, S. Lu, X. Tao, Y. Che, J.F. Chen, *ACS Appl. Mater. Interfaces* 7 (2015) 6093–6101.
- [68] Y. Wang, H.B. Fang, Y.Z. Zheng, R. Ye, X. Tao, J.F. Chen, *Nanoscale* 7 (2015) 19118–19128.
- [69] Q. Hou, Y. Zheng, J.-F. Chen, W. Zhou, J. Deng, X. Tao, *J. Mater. Chem.* 21 (2011) 3877.